Stable Dirac semimetal in the allotropes of group-IV elements

Wendong Cao,[1] Peizhe Tang,[2,*] Shou-Cheng Zhang,[2] Wenhui Duan,[1,3,4,†] and Angel Rubio[5,6,‡]

[1]*State Key Laboratory of Low-Dimensional Quantum Physics, Department of Physics, Tsinghua University, Beijing 100084, People's Republic of China*

[2]*Department of Physics, McCullough Building, Stanford University, Stanford, California 94305-4045, USA*

[3]*Institute for Advanced Study, Tsinghua University, Beijing 100084, People's Republic of China*

[4]*Collaborative Innovation Center of Quantum Matter, Beijing 100084, People's Republic of China*

[5]*Max Planck Institute for the Structure and Dynamics of Matter and Center for Free-Electron Laser Science, Luruper Chaussee 149, 22761 Hamburg, Germany*

[6]*Nano-Bio Spectroscopy group, Dpto. Física de Materiales, Universidad del País Vasco, Centro de Física de Materiales CSIC-UPV/EHU-MPC and DIPC, Av. Tolosa 72, E-20018 San Sebastián, Spain*

Three-dimensional topological Dirac semimetals represent a novel state of quantum matter with exotic electronic properties, in which a pair of Dirac points with a linear dispersion along all momentum directions exists in the bulk. Herein, by using first-principles calculations, we discover the metastable allotropes of Ge and Sn in the staggered layered dumbbell structure, named germancite and stancite, to be Dirac semimetals with a pair of Dirac points on their rotation axis. On the surface parallel to the rotation axis, a pair of topologically nontrivial Fermi arcs are observed and a Lifshitz transition is found by tuning the Fermi level. Furthermore, the quantum thin film of germancite is found to be an intrinsic quantum spin Hall insulator. These discoveries suggest novel physical properties and future applications of the metastable allotrope of Ge and Sn.

I. INTRODUCTION

The Dirac semimetals, whose low-energy physics can be described by the three-dimensional (3D) pseudorelativistic Dirac equation with a linear dispersion around the Fermi level [1], have attracted lots of attention in recent days, owing to their exotic physical properties [2–6] and large application potentials in the future [7–9]. Current studies mainly focus on two types of Dirac semimetals with both inversion symmetry and time-reversal (TR) symmetry. One is achieved at the critical point of a topological phase transition. This type of Dirac semimetal is not protected by any topology and can be gapped easily via small perturbations [10–12]. In contrast, the other type is protected by the uniaxial rotation symmetry [13], so is quite stable. Moreover, according to the parity of the states at the axis of C_n rotation, the symmetry protected Dirac semimetals can be further classified in two subclasses [14]. The first subclass has a single Dirac point (DP) at a time-reversal invariant momentum (TRIM) point on the rotation axis protected by the lattice symmetry [15,16], while the second one possesses nontrivial band inversion and has a pair of DPs on the rotation axis away from the TRIM points. For the materials of the second subclass (such as Na_3Bi [2,17], Cd_3As_2 [3,8,9,18–22], and some charge balanced compounds [23,24]), the nonzero $\mathbb{Z}_2$ number can be well defined at the corresponding two-dimensional (2D) plane of the Brillouin zone (BZ) [25,26]. Due to the nontrivial topology, these stable Dirac semimetals are regarded as a copy of Weyl semimetals [14]. Thus Fermi arcs are observed on the specific surfaces [27], and a quantum oscillation of the topological property

is expected to be achieved in a thin film with the change of thickness [3].

In spite of this successful progress, 3D Dirac semimetal materials either take uncommon lattice structures or contain heavy atoms, which are not compatible with current semiconductor industry. On the other hand, the group-IV elements, including C, Si, Ge, Sn, and Pb, have been widely used in electronics and microelectronics. Generally, for some of the group-IV elements, the diamond structure is one of the most stable 3D forms at ambient conditions. However, under specific experimental growth conditions, various allotropes with exotic physical and chemical properties are discovered experimentally. For example, the new orthorhombic allotrope of silicon, Si_{24}, is found to be a semiconductor with a direct gap of 1.3 eV at the Γ point [28]; and the 2D forms of silicene [29–31], germanene [32,33], and stanene [34–36] have been theoretically predicted to exist or experimentally grown on different substrates, which can be 2D topological insulators (TIs) and used as 2D field-effect transistors [37].

In this Rapid Communication, by using *ab initio* density functional theory (DFT) with a hybrid functional [38], we predict new 3D metastable allotropes for Ge and Sn with staggered layered dumbbell (SLD) structure, named germancite and stancite, and discover that they are stable Dirac semimetals with a pair of gapless DPs on the rotation axis of C_3 protected by the lattice symmetry. Similar to the conventional Dirac semimetals, such as Na_3Bi and Cd_3As_2, topologically nontrivial Fermi arcs can be observed on the surfaces parallel to the rotation axis in the germancite and stancite, and by tuning the Fermi level, we can observe a Lifshitz transition in the momentum space. More importantly for future applications, the thin film of the germancite is found to be an intrinsic 2D TI, and ultrahigh mobility and giant magnetoresistance can be expected in these compounds due to the 3D linear dispersion.

―――――――――
*peizhet@stanford.edu
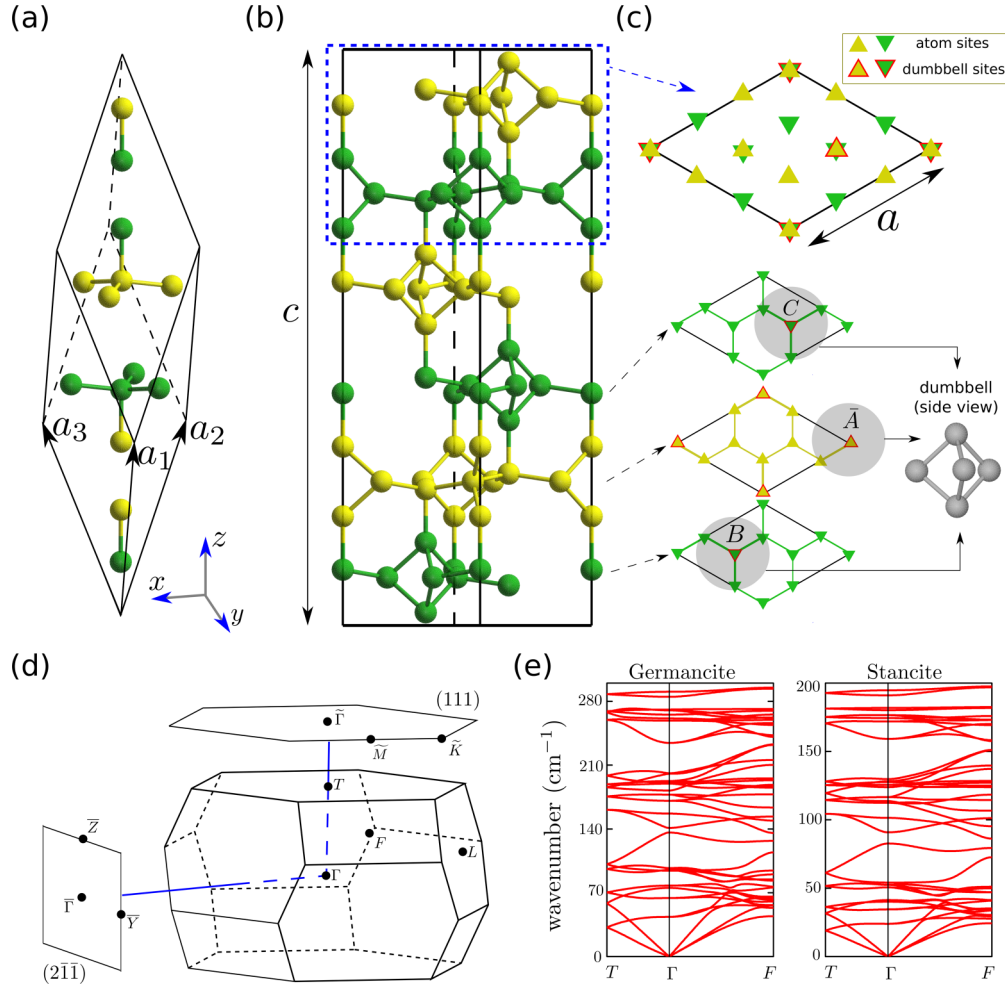
†dwh@phys.tsinghua.edu.cn

‡angel.rubio@mpsd.mpg.de

FIG. 1. (a) The unit cell of the SLD structure with three private lattice vectors set as $\mathbf{a_{1,2,3}}$. The balls in different colors stand for the same kind of atoms in different layers. (b) The side view and (c) top view of the SLD structure. The layers containing dumbbell (DB) structures are labeled. The letters (A,B,C) denote the positions of DB sites and the sign of bar is applied to distinguish between two trigonal lattices transformed to each other by inversion. As an example, the top view of two adjacent layers (marked by dashed blue lines) is shown. The DB structures are labeled by the grey shadow shown in the top view of a single layer, and the atoms in one DB structure are represented by grey balls. (d) The 3D Brillouin zone (BZ) of germancite and stancite. The four inequivalent TRIM points are Γ (0,0,0), L (0,π,0), F (π, π,0), and T (π, π, π). The hexagon and square, connected to Γ by blue lines, show the 2D BZs projected to (111) and ($2\bar{1}\bar{1}$) surfaces respectively, and the high-symmetry k points are labeled. (e) The phonon dispersion of germancite and stancite along high-symmetry lines of 3D BZ.

II. METHODS

The calculations were carried out by using DFT with the projector augmented wave method [39,40], as implemented in the Vienna *ab initio* simulation package [41]. A plane-wave basis set with a kinetic energy cutoff of 250 and 150 eV was used for germancite and stancite, respectively. The structure is allowed to fully relax until the residual forces are less than 1×10^{-3} eV/Å. The Monkhorst-Pack k points are $9 \times 9 \times 9$. With the relaxed structure, the electronic structure calculation of germancite and stancite using the hybrid functional HSE06 [38] has been done with and without SOC. Maximally localized Wannier functions [42] are constructed to obtain the tight-binding Hamiltonian for the Green's function method [43], which is used to calculate the surface electronic spectrum and surface states.

III. RESULTS

As shown in Fig. 1, the germancite and stancite share the same rhombohedral crystal structure with the space group of D_{3d}^6 ($R\bar{3}c$) [44], which contains the spacial inversion symmetry and C_3 rotation symmetry along the trigonal axis (defined as z axis). In one unit cell, fourteen atoms bond with each others to form six atomic layers; and in each layer, one dumbbell site can be observed. To clearly visualize the SLD structure in the germancite and stancite, we plot the side view of the hexagonal lattice shown in Fig. 1(b) and the top view from the (111) direction in Fig. 1(c). As the grey shadow shown, the layers containing dumbbell sites stack along the (111) direction in the order of $\cdots B\bar{A}C\bar{B}A\bar{C}\cdots$. The interlayer interaction is the covalent bonding between adjacent layers, whose bond lengths are almost equal to those of intralayer bonding (the difference
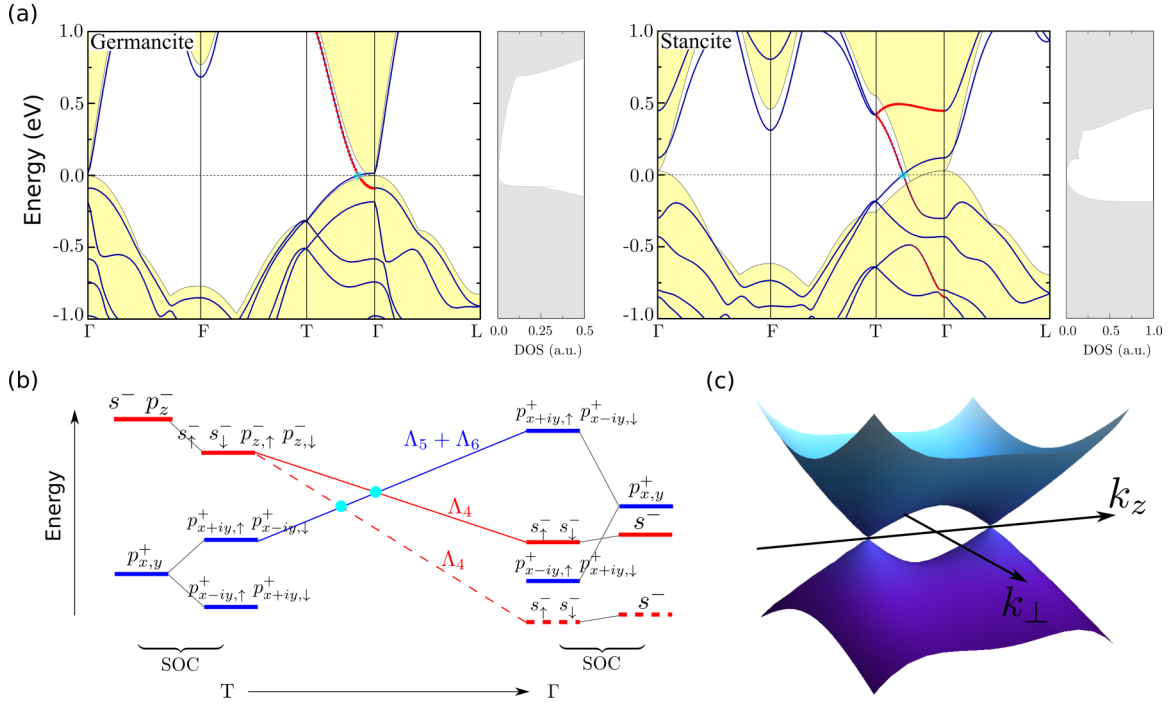
FIG. 2. (a) The band structures of germancite (left) and stancite (right) along high-symmetry lines with the corresponding DOS around the Fermi level (dashed horizontal line). In the k path T-Γ, the size of the red dots represents the contribution from the atomic s and p_z orbitals. The cyan dots are the Dirac points at $(0,0,k_{z0})$, where $k_{z0} \approx 0.08$ and $\approx 0.18\,\text{Å}^{-1}$, respectively. Shaded regions denote the calculated energy spectrum without SOC. (b) Schematic diagrams of the lowest conduction bands and highest valence bands from the T point to the Γ point for germancite and stancite. The black lines present the SOC effect at the T and Γ points. Between them, the red and blue lines denote doubly degenerate bands belonging to different irreducible representations, where the solid/dashed red line is for germancite/stancite. And the crossing points (solid cyan dots) correspond to those gapless Dirac points in (a), respectively. (c) Schematic band dispersion based on the effective $k \cdot p$ model for germancite and stancite. The $k_\perp$ direction refers to any axis perpendicular to the k_z direction in the momentum space and the color becomes warmer as the energy increases.

is about 0.03 Å). Meanwhile, different from the diamond structure, the tetrahedral symmetry is absent in the SLD structure and the coupling here is not a typical sp^3 hybridization. Furthermore, in order to test the structural stability, we calculate the phonon dispersion for the germancite and stancite shown in Fig. 1(e). It can be seen that the frequencies of all modes are positive over the whole Brillouin zone, which indicates that the SLD structures are thermodynamically stable. Furthermore, compared with the other experimentally discovered metastable allotropes of Ge and Sn [45–50], the germancite and stancite share the same order of magnetite of the mass density and cohesive energies (see Ref. [51] for details), so we expect that germancite and stancite could be composed in future experiments.

The calculated electronic structures of the germancite and stancite around the Fermi level are shown in Fig. 2(a), in which the solid lines and the yellow shadow stand for the bulk bands with and without spin-orbit coupling (SOC), respectively. It could be observed that when the SOC effect is not included, the germancite is a conventional semimetal whose bottom of the conduction bands and top of valence bands touch at the Γ point with the parabolic dispersions, while for stancite, it is a metal whose band touching at the Γ point is higher than the Fermi level. When the SOC effect is fully considered, our calculations indicate both germancite and stancite to be 3D Dirac semimetals with a pair of DPs in the trigonal rotation

axis [DP at $(0,0,\pm k_{z0})$]. Therefore the low-energy physics of this kind of materials can be described by the 3D Dirac-type Hamiltonian. And the schematic band structure based on the effective $k \cdot p$ model (see Ref. [51] for details) for germancite and stancite is shown in Fig. 2(c), in which the pair of 3D DPs is clearly seen.

To understand the physical origin of the 3D gapless Dirac fermions in the SLD structure, we plot the schematic diagram of the band evolution for the germancte and stancite in Fig. 2(b). In contrast to isotropic coupling in the diamond structure, the hybridizations in the layered SLD structure are anisotropic, in which the interlayer couplings are relatively weaker than intralayer couplings and the p_z and $p_{x\pm iy}$ states are split. Furthermore, based on our calculations, the kind of anisotropic coupling will further shift down the antibonding state of the s orbital, which is even lower than the bonding states of the $p_{x\pm iy}$ orbitals at the Γ point. So a band inversion occurs at the Γ point even without the SOC effect, and the SOC herein just removes the degeneracy of $p_{x\pm iy}$ orbitals around the Fermi level. In the 2D BZ which contains the Γ point and is perpendicular to the Γ-T direction, the nonzero $\mathbb{Z}_2$ topological number can be well defined. On the other hand, the C_{3v} symmetry along the Γ-T line contains one 2D (Λ_4) and two degenerate 1D (Λ_5, Λ_6) irreducible representations for its double space group [52]. As shown in Fig. 2(b), the two crossing bands at the Fermi level belong to $\Lambda_5 + \Lambda_6$ and Λ_4,
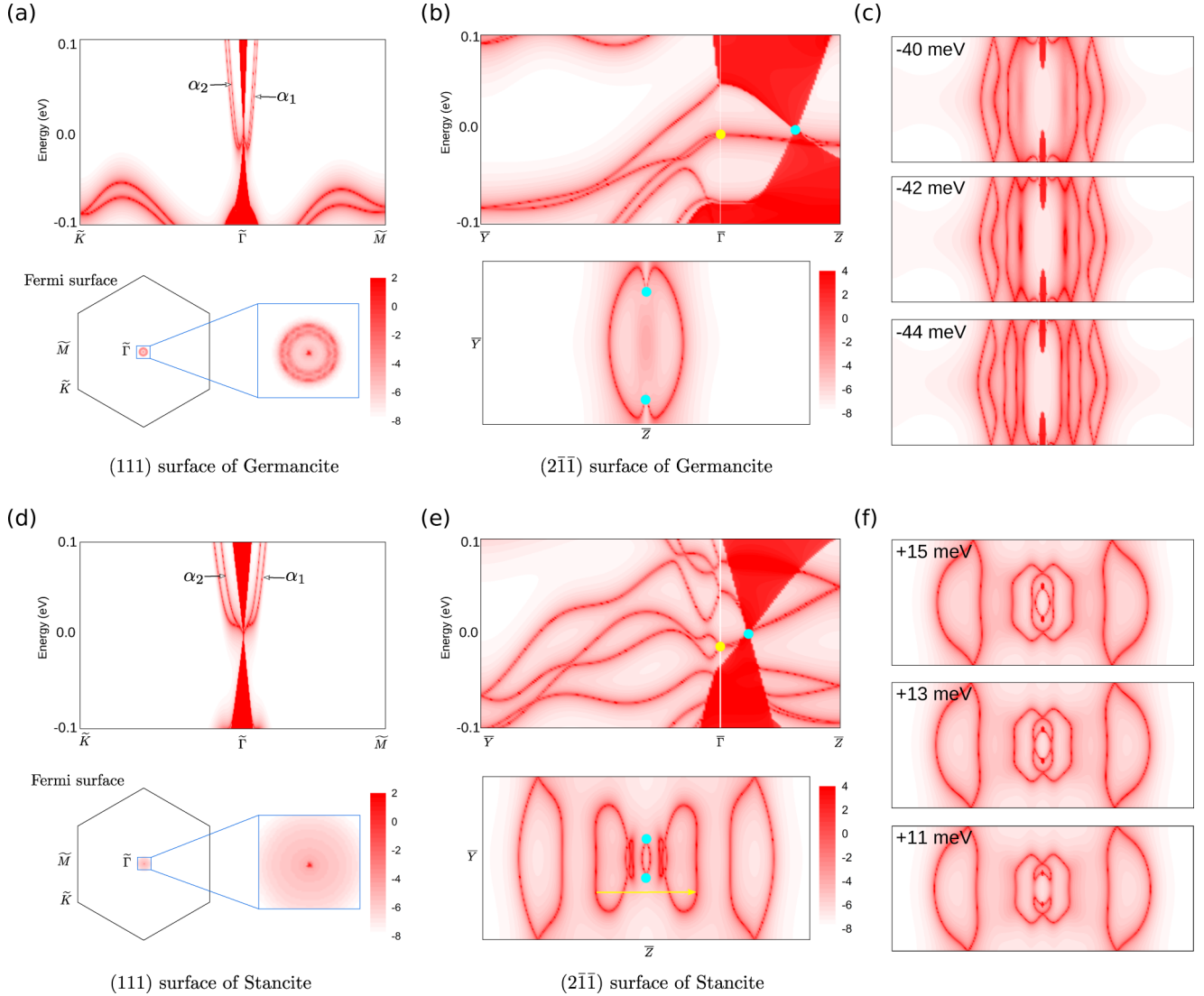
FIG. 3. The electronic spectrum on the (111) surface and its corresponding Fermi surface for (a) germanctie and (d) stancite, respectively. Two bulk DPs are projected to the $\widetilde{\Gamma}$ point. The electronic spectrum on the ($2\bar{1}\bar{1}$) surface and its corresponding Fermi surface for (b) germanctie and (e) stancite, respectively. The cyan dots label the projected DPs and the yellow dot represents the band crossing at the $\bar{\Gamma}$ point. On the Fermi surface, the Fermi arcs connect two projected DPs (cyan dots). For the stancite ($2\bar{1}\bar{1}$) surface, the constant-energy contour is at $\epsilon_f - 5.2$ meV, slightly away from the Fermi level, to distinguish the Fermi arcs. Stacking plots of constant-energy contours at different energies on the ($2\bar{1}\bar{1}$) surface of (c) germanctie and (f) stancite, respectively. The Fermi level is set to be zero.

respectively. So there is no coupling and a TR pair of 3D DPs can be observed at the Fermi level along the Γ-T direction.

Due to the nontrivial topology of 3D Dirac semimetals, the projected 2D DPs and Fermi arcs are expected to be observed on some specific surfaces for the germancite and stancite. As shown in Fig. 3, by using the surface Green's function method [43], we study the electronic spectrum on the (111) and ($2\bar{1}\bar{1}$) surfaces whose BZs are perpendicular and parallel to the Γ-T direction, respectively. For the BZ of the (111) surface, the pair of 3D DPs project to the $\widetilde{\Gamma}$ point as 2D Dirac cones [see Figs. 3(a) and 3(d)]; when the coupling between two projected 2D DPs is considered, a finite band gap could be easily obtained. Furthermore, besides the projected Dirac cones, we also observe trivial surface states in the germancite and stancite [$\alpha_{1,2}$ states in the Figs. 3(a) and 3(d)], which mainly originate from the dangling bonds on the (111) surface.

For the ($2\bar{1}\bar{1}$) surface of the germancite and stancite, the electronic structures are quite different. Because the BZ of ($2\bar{1}\bar{1}$) surface is parallel to the Γ-T direction, the pair of 3D DPs are projected to different points $(0,0,\pm\bar{k}_{z0})$, which are marked by the cyan dots in Figs. 3(b) and 3(e). Between the projected DPs, a pair of the Fermi arcs could be observed clearly, which share the helical spin texture and are not continuous at the projected points. This Fermi arcs originate from the nontrivial $\mathbb{Z}_2$ topology in the Dirac semimetals. On any 2D plane in the bulk whose BZ is perpendicular to the Γ-T direction with $-k_{z0} < k_z < k_{z0}$, the $\mathbb{Z}_2$ number is +1. Thus, in real space, a corresponding "edge state" exist on the boundary. In the moment space, the BZ of the "edge state" corresponds to the line parallel to $\bar{Y}$-$\bar{\Gamma}$-$\bar{Y}$ with $-\bar{k}_{z0} < \bar{k}_z < \bar{k}_{z0}$, and its Fermi surface should be two points. After concluding all the contributions of planes with $\mathbb{Z}_2 = 1$, the Fermi surface
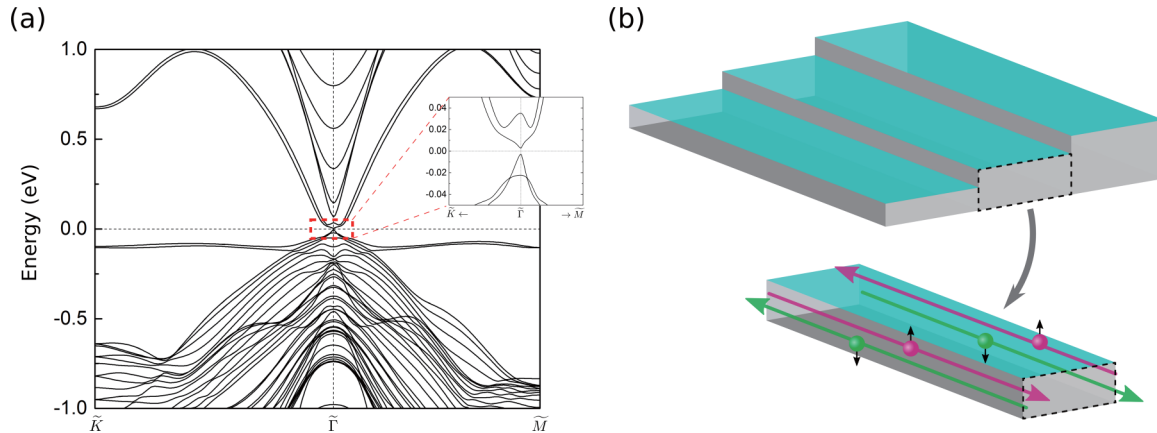
FIG. 4. (a) Band structure of 16-layer germancite (111) film. The topologically nontrivial gap at the $\widetilde{\Gamma}$ can be seen in the inset. (b) Schematic device consisting of three germancite thin films with different thickness. The middle one is a QSH insulator, whereas the other two are topologically trivial. In the lower panel, the purple and green vectors stand for the spin-polarized current at the interfaces.

becomes a pair of the Fermi arcs on the BZ of $(2\bar{1}\bar{1})$ surface which connect the projected DPs. At the same time, on the $(2\bar{1}\bar{1})$ surface, other surface states contributed by the dangling bond also exist. Via tuning the Fermi level, we could observe a hybridization between the nontrivial surface states and Fermi arcs [see Figs. 3(c) and 3(f)], so a Lifshitz transition is found on the Fermi surface. Additionally, because the Fermi surface contours on the $(2\bar{1}\bar{1})$ surface contain roughly the same wave vector [see the yellow arrow in Fig. 3(e)], a charge density wave or surface reconstruction can be observed here. However, the surface coupling will not break the TR symmetry or change the bulk topology, the pair of Fermi arcs always exist.

IV. DISCUSSION AND CONCLUSION

Because of the compatibility with the traditional semiconductor devices and dissipationless edge transport, the realization of the quantum spin Hall (QSH) effect in the thin film of Ge attracts lots of attention recently. In a recent proposal [53], the nontrivial topology of the 2D thin film is induced by the large build-in electric field in the semiconductor interface, which may be difficult to control in real experiments. On the other hand, due to the nontrivial topology of the Dirac semimetal, the germancite (111) film may provide another opportunity for obtaining the QSH insulator. With the $k \cdot p$ model of the film, we can prove that the germancite (111) film oscillates between the normal insulator and the QSH insulator with increasing thickness (see Ref. [51] for details). So if we build the film with a proper thickness along the (111) direction, the band inversion may be restored at the $\widetilde{\Gamma}$ point and this thin film would become a QSH insulator. Figure 4(a) shows the electronic structure for germancite (111) film with a thickness of 72.7 Å (i.e., 16 layer [54]), which is calculated by using the tight-binding method with the Wannier function basis. A small band gap (5.6 meV) opens at the $\widetilde{\Gamma}$ point [55]. To confirm its nontrivial topological nature, we calculate its $\mathbb{Z}_2$ number from the evolution of the Wannier charge centers (see Supplemental Material Information [51] for details). So we find that the 16-layer germancite (111) film is a 2D TI without applying an external electric field. Moreover, helical edge states can be realized in germancite (111) films by tuning the thickness. As shown schematically in Fig. 4(b), there are three films of different thickness (from left to right). The middle film is a QSH insulator while the other two are normal insulators. The helical edge states appear at the phase boundary.

In conclusion, from DFT calculations with the hybrid functional, we predict that germancite and stancite with the SLD structure are stable topological Dirac semimetals protected by the rotation symmetry. It is found that the Fermi arcs coexist with the trivial surface states on the surface plane parallel to the rotation axis of C_3, and a Lifshitz transition is observed when the Fermi level is tuned. Furthermore, we discover that the (111) thin film of the germancite is a 2D TI without applying the external electric field, which is important for future applications. Experimentally, metastable allotropes of germanium have been synthesized through the oxidation of Ge_9^{4-} Zintl anions in ionic liquids under ambient conditions [45]. Owing to similar density and cohesive energy, we expect that germancite and stancite could be synthesized via similar methods in the future.

[1] A. A. Burkov, M. D. Hook, and L. Balents, Phys. Rev. B **84**, 235126 (2011).

[2] Z. Wang, Y. Sun, X.-Q. Chen, C. Franchini, G. Xu, H. Weng, X. Dai, and Z. Fang, Phys. Rev. B **85**, 195320 (2012).

[3] Z. Wang, H. Weng, Q. Wu, X. Dai, and Z. Fang, Phys. Rev. B **88**, 125427 (2013).

[4] R. Li, J. Wang, X.-L. Qi, and S.-C. Zhang, Nat. Phys. **6**, 284 (2010).

[5] A. C. Potter, I. Kimchi, and A. Vishwanath, Nat. Commun. **5**, 5161 (2014).

[6] S. A. Parameswaran, T. Grover, D. A. Abanin, D. A. Pesin, and A. Vishwanath, Phys. Rev. X **4**, 031035 (2014).

[7] A. A. Abrikosov, Phys. Rev. B **58**, 2788 (1998).

[8] T. Liang, Q. Gibson, M. N. Ali, M. Liu, R. J. Cava, and N. P. Ong, Nat. Mater. **14**, 280 (2015).

[9] L. P. He, X. C. Hong, J. K. Dong, J. Pan, Z. Zhang, J. Zhang, and S. Y. Li, Phys. Rev. Lett. **113**, 246402 (2014).

[10] T. Sato, K. Segawa, K. Kosaka, S. Souma, K. Nakayama, K. Eto, T. Minami, Y. Ando, and T. Takahashi, Nat. Phys. **7**, 840 (2011).

[11] L. Wu, M. Brahlek, R. Valdés Aguilar, A. V. Stier, C. M. Morris, Y. Lubashevsky, L. S. Bilbro, N. Bansal, S. Oh, and N. P. Armitage, Nat. Phys. **9**, 410 (2013).

[12] J. Liu and D. Vanderbilt, Phys. Rev. B **88**, 224202 (2013).

[13] C. Fang, M. J. Gilbert, and B. A. Bernevig, Phys. Rev. B **86**, 115112 (2012).

[14] B.-J. Yang and N. Nagaosa, Nat. Commun. **5**, 4898 (2014).

[15] S. M. Young, S. Zaheer, J. C. Y. Teo, C. L. Kane, E. J. Mele, and A. M. Rappe, Phys. Rev. Lett. **108**, 140405 (2012).

[16] J. A. Steinberg, S. M. Young, S. Zaheer, C. L. Kane, E. J. Mele, and A. M. Rappe, Phys. Rev. Lett. **112**, 036403 (2014).

[17] Z. K. Liu *et al.*, Science **343**, 864 (2014).

[18] Z. K. Liu *et al.*, Nat. Mater. **13**, 677 (2014).

[19] S. Borisenko, Q. Gibson, D. Evtushinsky, V. Zabolotnyy, B. Büchner, and R. J. Cava, Phys. Rev. Lett. **113**, 027603 (2014).

[20] H. Yi *et al.*, Sci. Rep. **4**, 6106 (2014).

[21] S. Jeon, B. B. Zhou, A. Gyenis, B. E. Feldman, I. Kimchi, A. C. Potter, Q. D. Gibson, R. J. Cava, A. Vishwanath, and A. Yazdani, Nat. Mater. **13**, 851 (2014).

[22] A. Narayanan *et al.*, Phys. Rev. Lett. **114**, 117201 (2015).

[23] Q. D. Gibson, L. M. Schoop, L. Muechler, L. S. Xie, M. Hirschberger, N. P. Ong, R. Car, and R. J. Cava, Phys. Rev. B **91**, 205128 (2015).

[24] Y. Du, B. Wan, D. Wang, L. Sheng, C.-G. Duan, and X. Wan, Sci. Rep. **5**, 14423 (2015).

[25] T. Morimoto and A. Furusaki, Phys. Rev. B **89**, 235127 (2014).

[26] E. V. Gorbar, V. A. Miransky, I. A. Shovkovy, and P. O. Sukhachov, Phys. Rev. B **91**, 121101 (2015).

[27] S.-Y. Xu *et al.*, Science **347**, 294 (2015).

[28] D. Y. Kim, S. Stefanoski, O. O. Kurakevych, and T. A. Strobel, Nat. Mater. **14**, 169 (2015).

[29] S. Cahangirov, M. Topsakal, E. Aktürk, H. Şahin, and S. Ciraci, Phys. Rev. Lett. **102**, 236804 (2009).

[30] S. Cahangirov, M. Audiffred, P. Tang, A. Iacomino, W. Duan, G. Merino, and A. Rubio, Phys. Rev. B **88**, 035432 (2013).

[31] S. Cahangirov, V. O. Özçelik, L. Xian, J. Avila, S. Cho, M. C. Asensio, S. Salim, and A. Rubio, Phys. Rev. B **90**, 035448 (2014).

[32] E. Dávila, L. Xian, S. Cahangirov, A. Rubio, and G. Le Lay, New J. Phys. **16**, 095002 (2014).

[33] C. Si, J. Liu, Y. Xu, J. Wu, B.-L. Gu, and W. Duan, Phys. Rev. B **89**, 115429 (2014).

[34] P. Tang, P. Chen, W. Cao, H. Huang, S. Cahangirov, L. Xian, Y. Xu, S.-C. Zhang, W. Duan, and A. Rubio, Phys. Rev. B **90**, 121408 (2014).

[35] Y. Xu, B. Yan, H.-J. Zhang, J. Wang, G. Xu, P. Tang, W. Duan, and S.-C. Zhang, Phys. Rev. Lett. **111**, 136804 (2013).

[36] F.-F. Zhu, W.-J. Chen, Y. Xu, C.-L. Gao, D.-D. Guan, C.-H. Liu, D. Qian, S.-C. Zhang, and J.-F. Jia, Nat. Mater. **14**, 1020 (2015).

[37] L. Tao, E. Cinquanta, D. Chiappe, C. Grazianetti, M. Fanciulli, M. Dubey, A. Molle, and D. Akinwande, Nat. Nanotech. **10**, 227 (2015).

[38] J. Heyd, G. E. Scuseria, and M. Ernzerhof, J. Chem. Phys. **118**, 8207 (2003).

[39] P. E. Blöchl, Phys. Rev. B **50**, 17953 (1994).

[40] G. Kresse and D. Joubert, Phys. Rev. B **59**, 1758 (1999).

[41] G. Kresse and J. Furthmüller, Phys. Rev. B **54**, 11169 (1996).

[42] A. A. Mostofi, J. R. Yates, Y.-S. Lee, I. Souza, D. Vanderbilt, and N. Marzari, Comput. Phys. Commun. **178**, 685 (2008).

[43] M. P. L. Sancho, J. M. L. Sancho, and J. Rubio, J. Phys. F **15**, 851 (1985).

[44] S. Cahangirov, V. O. Özçelik, A. Rubio, and S. Ciraci, Phys. Rev. B **90**, 085426 (2014).

[45] A. M. Guloy, R. Ramlau, Z. Tang, W. Schnelle, M. Baitinger, and Y. Grin, Nature (London) **443**, 320 (2006).

[46] F. Kiefer, V. Hlukhyy, A. J. Karttunen, T. F. Fässler, C. Gold, E.-W. Scheidt, W. Scherer, J. Nyléna, and U. Häussermannd, J. Mater. Chem. **20**, 1780 (2010).

[47] B. C. Johnson, B. Haberl, S. Deshmukh, B. D. Malone, M. L. Cohen, J. C. McCallum, J. S. Williams, and J. E. Bradby, Phys. Rev. Lett. **110**, 085502 (2013).

[48] Z. Zhao *et al.*, J. Am. Chem. Soc. **134**, 12362 (2012).

[49] A. Ceylan, A. E. Gumrukcu, N. Akin, S. Ozcan, and S. Ozcelik, Mater. Sci. Semicond. Process. **40**, 407 (2015).

[50] C. S. Menoni, J. Z. Hu, and I. L. Spain, Phys. Rev. B **34**, 362 (1986).

[51] See Supplemental Material at http://link.aps.org/supplemental/10.1103/PhysRevB.93.241117 for more details about the effective $k \cdot p$ model, topological properties of germancite (111) films, and stability analysis.

[52] G. Koster, *Properties Of The Thirty-two Point Groups*, Massachusetts Institute of Technology Press Research Monograph (M.I.T. Press, Cambridge, Massachusetts, United States, 1963).

[53] D. Zhang, W. Lou, M. Miao, S.-C. Zhang, and K. Chang, Phys. Rev. Lett. **111**, 156402 (2013).

[54] According to our calculations in Ref. [51], we find that both the four- and 16-layer film have a nontrivial band order at the $\tilde{\Gamma}$ point. However, the former one has a negative indirect gap. Therefore we choose the 16-layer germancite (111) film to demonstrate the existence of QSH insulator in germancite (111) films .

[55] Under realistic conditions, the electronic structure of the germancite (111) films (such as the 16-layer film) may change due to real surface potentials or other effects. But as long as the germancite bulk remains a Dirac semimetal, we can infer that the existence of QSH insulator in its (111) films is robust from the theoretical analysis of the $k \cdot p$ model of the films in Ref. [51] .